BIOCHEMISTRY
including biophysical chemistry & molecular biology

ARTICLE

pubs.acs.org/biochemistry

Interaction of Nitric Oxide with Catalase: Structural and Kinetic Analysis

Namrta Purwar,[†] Jennifer M. McGarry,[‡] Joshua Kostera,[‡] A. Andrew Pacheco,[*,‡] and Marius Schmidt[*,†]

[†]Department of Physics, University of Wisconsin—Milwaukee, 1900 East Kenwood Boulevard, Milwaukee, Wisconsin 53211, United States

[‡]Department of Chemistry and Biochemistry, University of Wisconsin—Milwaukee, 3210 North Cramer Street, Milwaukee, Wisconsin 53211, United States

Supporting Information

ABSTRACT: We present the structures of bovine catalase in its native form and complexed with ammonia and nitric oxide, obtained by X-ray crystallography. Using the NO generator 1-(*N*,*N*-diethylamino)diazen-1-ium-1,2-diolate, we were able to generate sufficiently high NO concentrations within the catalase crystals that substantial occupation was observed despite a high dissociation rate. Nitric oxide seems to be slightly bent from the heme normal that may indicate some iron(II) character in the formally ferric catalase. Microspectrophotometric investigations inline with the synchrotron X-ray beam reveal photoreduction of the central heme iron. In the cases of the native and ammonia-complexed catalase, reduction is accompanied by a relaxation phase. This is likely not the case for the catalase NO complex. The kinetics of binding of NO to catalase were investigated using NO photolyzed from *N*,*N*′-bis(carboxymethyl)-*N*,*N*′-dinitroso-*p*-phenylenediamine using an assay that combines catalase with myoglobin binding kinetics. The off rate is 1.5 s^{-1}. Implications for catalase function are discussed.

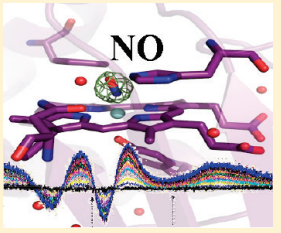

Nitric oxide is known for its role in bioregulatory processes like vasodilatation, macrophage-induced cytostatis, cytotoxicity, and neurotransmission.[1−7] It also behaves as a ubiquitous signaling molecule operating through nitrosylation.[8] Further S-nitrosylation can regulate protein−protein interactions and may have an impact on cellular signaling networks.[9] Transition metal nitrosyl complexes within metalloenzymes play central roles in the biological chemistry of NO.[10] In our laboratories, we are investigating a number of metalloenzymes involved in NO trafficking. Because many of the nitrosylated metalloenzyme intermediates of interest to us are metastable, we have had to develop a number of methods for detecting such transient species (see, for example, refs 11−13). Herein, we report on a methodology that allowed us to obtain the crystal structure of nitrosylated catalase, which is kinetically labile. This methodology should be readily applicable to the crystallographic analysis of other labile nitrosylated metalloenzymes.

Catalase (EC 1.11.1.6) is a heme protein, which is found in many bacteria and almost all plants and animals.[14] It catalyzes the disproportionation of toxic hydrogen peroxide into oxygen and water (eq 1)

$$2H_2O_2 \rightarrow 2H_2O + O_2 \qquad (1)$$

a reaction of great importance to all aerobically respiring organisms. Reactive oxygen species (ROS) like H_2O_2 and HO_2 (superoxide) are inevitable byproducts of aerobic respiration, necessitating specialized enzymes for their elimination.[15−17] Typical examples for mammalian catalases are bovine liver and human erythrocyte catalase.[18] Bovine liver catalase was crystallized for the first time in 1937[19] and bovine erythrocyte catalase in 1969.[20]

The structure of bovine liver catalase (Cat) was determined initially in 1981,[14] and refinements were subsequently reported by Reid et al. in 1981[21] and Ko et al. in 1999.[22] This catalase is a tetramer.[23,24] Each monomer (∼60 kDa) consists of 507 amino acid residues and contains a heme group with the iron in the ferric state.[25−27] Structures of catalases containing a variety of ligands bound at the active site have also been reported: azide,[28] formate,[29] oxo (compounds I and II),[30,31] and cyanide and 3-amino-1,2,4-Triazol.[32] Such active site adducts were prepared primarily to provide structural information about intermediates important to the catalytic mechanism. Herein, we report the structure of Cat complexed with nitric oxide, along with a microspectrophotometric analysis of the crystals during X-ray exposure. NO has been shown to be a competitive inhibitor of Cat, which could be physiologically significant.[33] The structure could also potentially yield insights about the Cat-H_2O_2 adduct, which is not sufficiently long-lived to be structurally characterized within the active enzyme. The microspectrophotometric analysis reveals the oxidation state of the active site that is determined crystallographically. Cat-NO complexes had not been previously characterized by X-ray crystallography because NO tends to dissociate rapidly from the active site, complicating data collection. We also report new values for the rate constant

Received: January 25, 2011
Revised: April 26, 2011
Published: April 27, 2011

Scheme 1. Molecular Structure of DEANO and Its Decomposition into Two NOs and Diethylamine

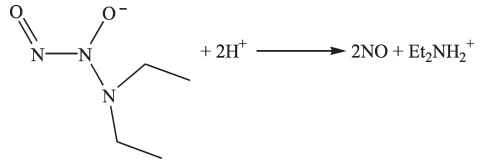

DEANO

Scheme 2. Molecular Structure of BNN and Its Photochemical Release of NO under Reducing Conditions

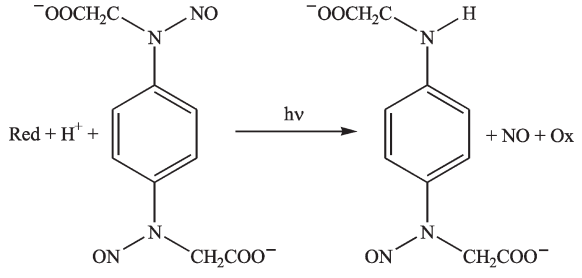

BNN

(k_{off}) governing dissociation of NO from Cat, and the associated thermodynamic Cat-NO binding constant ($K_{Cat\text{-}NO}$).

MATERIALS AND METHODS

Materials. Bovine liver catalase (Cat) was obtained from Sigma (C3155), as was horse skeletal muscle myoglobin (Mb). As obtained from Sigma, Mb is in the aquomet (Fe^{III}) form, but in our experiments, it was reduced as described below. Other than reduction, Mb was used without further manipulation. Cat on the other hand was purified using a Superdex 200 (GE) column. Fractions with a 405 nm to 276 nm absorption ratio of >7 were pooled. The Cat concentration was determined using the extinction coefficient of 420 cm^{-1} L $mmol^{-1}$ at 405 nm (for the tetramer).[21,34] To the concentrated Cat solution used in the crystallographic experiments was added 1−5 wt % NH_4OH (30% in water). Methyl viologen dichloride (MV_{ox}) was obtained from Acros and sodium dithionite from Aldrich. The nitric oxide generators 1-(*N*,*N*-diethylamino)diazen-1-ium-1,2-diolate [DEANO (Scheme 1)] and *N*,*N*′-bis(carboxymethyl)-*N*,*N*′-dinitroso-*p*-phenylenediamine [BNN (Scheme 2)] were prepared using methods previously described in refs 13 and 35. All other reagents were obtained from Fisher.

Crystallographic Analysis. *Crystallization.* Three different Cat crystal forms were prepared. Catalase was initially crystallized by the hanging drop vapor diffusion method, using conditions previously reported by Ko et al.[22] Four microliters of the concentrated protein (12−13 mg/mL, containing NH_4OH as described above) was mixed with an equal volume of the reservoir solution consisting of 45−60 mM magnesium formate. After 2−3 weeks, crystals with a typical size of 100 μm × 100 μm × 200 μm were obtained. These crystals are henceforth termed the Cat-NH_3 form. We obtained a second crystal preparation by soaking the Cat-NH_3 crystals overnight in an 80 mM magnesium formate solution (pH 6.7) and then washing them two more times with the same solution. We refer to the crystals thus obtained as Cat-5 crystals. Finally, we obtained crystals of the Cat-NO adduct by soaking the Cat-5 crystals for 5 min in pH 6.5 solutions containing 80 mM magnesium formate and 150 mM Bis-Tris as buffers, and DEANO at concentrations varying from 10 to 200 mM. To minimize the escape of NO into the atmosphere during the crystal nitrosylation process, we used the special apparatus shown in Figure 1. This apparatus consists simply of two glass plates with the mating surfaces ground to provide a very tight seal. The lower glass plate also has a hemispherical depression with a capacity of ∼200 μL. In any given experiment, a Cat-5 crystal was placed in the depression, which was then filled completely with the buffer/DEANO mixture, and the depression quickly capped with the top plate to prevent NO from leaving the cavity. A heavy weight was placed on top of the top plate to maintain the high internal pressure.

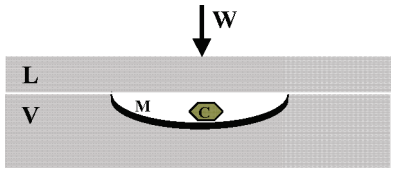

Figure 1. Schematic diagram of the apparatus used to generate NO from DEANO. Abbreviations: V, glass vessel containing a 200 μL cavity; L, glass lid; M, mother liquor; W, weight used to prevent NO from leaking from the glass vessel. A Cat crystal is colored green.

Crystal Freezing. The crystals obtained under each of the three conditions were soaked for ∼20 s in a cryobuffer containing 20% polyethylene glycol 4000, 20% sucrose, and 50 mM Tris (pH 8.5). The crystals were mounted in a loop and shock-frozen at 100 K using a Cryojet (Oxford Diffraction). For the Cat-NO crystals, it was imperative to move quickly between removing the crystals from the pressure apparatus and freezing them in the Cryojet. NO will begin to diffuse out of the crystal as soon as the pressure is released, and NO occupancy at the active site will drop to unusable levels within ∼10 min unless the crystal is frozen.

Data Collection. Data were collected at BioCARS 14-BMC (Advanced Photon Source, Argonne National Lab, Argonne, IL). For single crystals of Cat-NH_3, Cat-5, and Cat-NO, complete data sets were collected using 13.8 keV X-ray radiation (λ = 0.9 Å). Reflection intensities were recorded on a charge-coupled device area detector (ADSC Q315). For each data set, the crystals were rotated through 180° in steps of 0.5° to cover the reciprocal space.

Data Analysis and Refinement. Data were indexed and integrated with MOSFLM[36] and scaled with the CCP4 program SCALA.[37,38] Because our crystals were orthorhombic, we used model 4BLC from the Protein Data Bank (PDB)[39] for a molecular replacement. This model was also determined from an orthorhombic crystal form of Cat[22] and could be used directly as the starting model for a refinement using CNS.[40] To prepare an initial model, we removed the NADPH molecules as well as the water molecules from the starting model. For each crystal form, we used the same refinement protocol. First, a rigid body refinement was performed at 3.0 Å, followed by simulated annealing using a 2000 K protocol to full resolution. After that, positional conventional refinement was used until convergence was reached. Finally, the *B* factors were determined using 40-step restrained *B* factor refinement. For inspection of the Fourier maps, "Xfit" was used (xtalview package[41]).

Water Search. Water molecules were searched up to the 3σ level and added to the molecular structure. Special care was taken during the water search not to insert a water molecule at the sixth coordination site of the iron. After insertion of all the water molecules, the positions of all atoms were refined using conventional refinement. Inspection of sigmaA-weighted $2mF_{obs} - DF_{calc}$ and $mF_{obs} - DF_{calc}$ maps revealed misorientations of several amino acid side chains, which were manually reoriented into the electron density maps using Xfit. Refinement was repeated and the model corrected until no obvious misorientations could be detected. To determine the presence and orientation of any putative sixth iron ligand, the $2F_{obs} - F_{calc}$ electron density maps and the $F_{obs} - F_{calc}$ difference maps were examined in the vicinity of the heme iron. Once a positive feature had been identified, the $F_{obs} - F_{calc}$ difference electron density was integrated to calculate the total number of electrons at this site using Probe.[42]

Insertion of NO and NH_3. For Cat-NH_3, a positive electron density at the sixth coordination site was interpreted as NH_3, whereas for Cat-NO, a NO molecule was inserted into the electron density (see Results). Both the NO and the NH_3 were patched with the nitrogen atom to the iron at a distance of 1.9 Å using weak bond length restraints (50 kcal mol^{-1} $Å^{-2}$). The NO was oriented parallel to the heme normal with a very weak Fe−N−O angular restraint (7 kcal mol^{-1} rad^{-2}). The models were refined conventionally against their respective X-ray structure.

B Factor Averaging. The occupancy and *B* factor are usually hard to refine at nonatomic resolution. Because the electron count for the NO in Cat-NO indicated that not all Cat molecules in the crystal have an equal amount of NO bound, occupational refinement becomes necessary in addition to *B* factor refinement. For this, we alternated *B* factor and occupational refinement. First, the *B* factors for the N and O atoms of the NO determined from the conventional refinement (plus that of the iron and the four heme nitrogens) were averaged and assigned to both N and O. Then, the occupancy was refined for each individual NO using the grouped occupational refinement option in CNS. After that, the *B* factors for the NO molecules were refined again. This cycle was repeated until convergence was reached. In Cat-NH_3, we propose that ammonia is bound to the iron (see Results). The occcupancy and *B* factor for this crystal form were refined using a procedure similar to that just described for Cat-NO.

Geometry. To determine the orientation of the sixth axial ligand at the active site of Cat-NO, the tilt (τ) angle, the bend angle (ϕ), and the tilt and bend angle (α) were calculated with respect to the normal of the heme plane[43] (Figure 2). To compare the geometries of all four hemes in the three Cat structures, we determined the iron out of plane distance using Planefit.[43]

Microspectrophotometric Analysis of Cat Crystals during X-ray Irradiation. A microspectrophotometer (4DX) equipped with a deuterium/tungsten light source (DH2000, Ocean Optics) and a USB mini-spectrometer (USB 2000, Ocean Optics) available at BioCARS was mounted inline with the X-ray beam at BioCARS 14-BMC. During X-ray exposure (monochromatic flux of $\sim 5 \times 10^{11}$ photons/s), the absorption spectra of the three different catalase species were recorded at 100 K for up to 10 min in intervals of 10 s. Difference spectra were generated by subtracting the time-dependent spectra from the reference spectrum recorded before X-ray exposure. The absolute differences were integrated from 400 to 800 nm and plotted as a function of exposure time. Data were fitted empirically by functions that consist either of a single exponential, a sum of two exponentials, or an exponential and a linear phase.

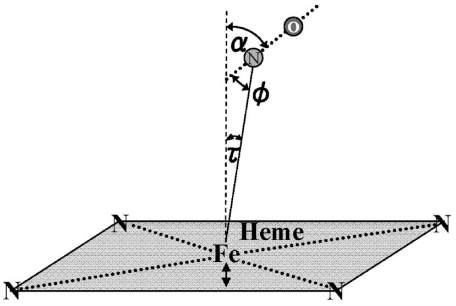

Figure 2. Tilt (τ), bend (ϕ), and tilt and bend (α) angles for the NO bound to the heme iron in Cat-NO. The heme plane is defined by the four porphyrin nitrogens. A double-headed arrow marks potential iron out of plane displacements.

Kinetic Analysis of Dissociation of NO from Cat-NO. *Sample Preparation.* All solutions were prepared and manipulated in a nitrogen-filled glovebox. Stock solutions were prepared daily and stored in a refrigerator at 4 °C until needed. All experiments were performed in solutions buffered with phosphate (μ = 50 mM, pH 7.4). Samples for any given experiment were prepared by mixing stock solutions of buffer, MV_{ox}, dithionite, BNN, Cat, and Mb in a 1.5 mL microcentrifuge tube, to give a total volume of 150 μL. The total concentration of MV in each sample was always 63 μM, and enough dithionite was added to reduce 25−45 μM of this to the monocation radical form (MV_{red}). The added dithionite also reduced aquometMb to the Fe^{II} form. The concentrations of the remaining reagents were 370−700 μM for BNN, 8.5−21 μM for Mb, and 11−15 μM for Cat. Once thoroughly mixed, the reaction mixtures were transferred to a 3 mm × 3 mm quartz fluorescence cuvette, fitted with a glass gastight stopper. The exact concentrations of all the reagents in the cuvette were determined by UV−vis spectroscopy using a previously described methodology.[44]

Data Collection and Instrumentation. Routine UV−vis spectra were recorded using a CARY 50 spectrophotometer (Varian) that was installed in the glovebox. Nitric oxide was photogenerated in situ from BNN using a methodology previously described[11−13,45] and summarized in Scheme 2. Briefly, photochemical fragmentation of BNN was initiated with a 10 ns, 308 nm, 6.0 mJ pulse from a XeCl excimer laser (TUI, Existar 200). This generated 1 equiv of free NO, which then reacted with Cat and Mb as described in Results. An OLIS RSM-1000 spectrophotometer was used to monitor the absorbance changes induced by the laser pulse. The configuration of the laser and spectrophotometric equipment has been described in general terms elsewhere.[11,13] All data were collected with the OLIS RSM-1000 in rapid-scanning mode (monochromator entrance slit width of 0.6 mm, scanning slit width of 0.2 mm, and exit slit width of 0.12 mm), which allows complete spectra to be obtained in 1 ms.

Data Analysis. Data were analyzed using the commercially available software packages Microcal Origin version 6.0 (Microcal Software, Inc.) and Mathcad 13 (Mathsoft Engineering and Education, Inc.). Changes in the complete spectra obtained using the Olis RSM as a function of time were analyzed using a previously described methodology.[11,44]

RESULTS

Crystal Structures. All the crystal forms obtained proved to be orthorhombic in space group $P2_12_12_1$. The unit cell dimensions vary slightly depending on the crystal form, in the following ranges: a = 83−86 Å, b = 139−140 Å, and c = 228−229 Å (Table 1). Multiple data sets were collected for each crystal form (see below), and the best one was picked on the basis of resolution, a low degree of mosaicity, and low R_{sym} values. Data typically extended to 1.9 Å and better and were more than 90% complete with an R_{sym} of <10%.

Ammonia-Bound Catalase (Cat-NH_3). The initial model prepared from PDB entry 4BLC (see above) was refined to 1.99 Å with an R value of 23.7%. The structure is shown in Figure 3A. Earlier studies have shown that Cat typically incorporates one tightly bound NADPH per subunit,[34,46] and an earlier structure obtained under the same conditions as ours revealed a bound NADPH group. However, our structure showed no electron density for the NADPH in the same region (Figure 3B), from which we conclude that the NADPH was lost during purification by size exclusion. After addition of all water molecules to the structure, the R value decreased to 16.8%. A strong positive electron density feature was present in the difference map ($mF_{obs} - DF_{calc}$) of Cat-NH_3, near the heme iron (Figure 4A). Because high concentrations of ammonium were present during the crystallization, we propose that the electron density arises from an ammonia molecule bound to each of the hemes. For each of the four hemes, the integrated electron count at the sixth coordination site is ∼9 e^-, which supports our proposal that NH_3 molecules are present there. NH_3 was placed into the electron density at a distance of 1.9 Å, and its position was refined. The occupancy of the NH_3 molecule refined to ∼1.0 for all four subunits. The iron out of plane distance (Figure 4A) was approximately ±0.05 Å for all hemes; hence, the iron is almost in plane. The model precision was 0.18 Å as estimated by a Luzzati plot (see, for example, ref 47).

Five-Coordinate Cat-5. The final model of Cat-NH_3 was used as a starting model to refine Cat-5. After the ammonia molecule at the sixth coordination site of the iron had been removed, as well as the water molecules, the model was refined to 1.9 Å. Inclusion of water lowered the R value to 22.1%. No positive density appeared at the heme active site (Figure 4B). Via integration of the faint electron density features around the sixth coordination site, the counted number of electrons was found to be <1.0 on average (Table 1). This demonstrates that NH_3 was successfully removed from this crystal form, leaving a vacant sixth coordination site at the heme.

Cat-NO Structure. The amount of NO needed to observe significant binding to the catalase crystals was optimized by testing different concentrations of DEANO, from 10 to 200 mM. DEANO concentrations of >100 mM gave satisfactory results, with more than 50% NO occupancy in the heme active site pocket. Data were collected to 1.88 Å (Table 1). The ammonia-free (Cat-5) structure without the water molecules was used as the initial model for the refinement. After water molecules had been inserted, the R value decreased to 18.6%. A positive electron density feature appeared at the sixth coordination site of the heme iron (Figure 4C), which was absent in Cat-5. This positive electron density was identified as a NO molecule. The refined NO occupancy is ∼55% on average (Table 1). Interestingly, a single water molecule was observed in the vicinity of the NO for all four hemes in this case. This seems to be important in defining the binding geometry of the NO with respect to the heme plane (see Discussion). The NO is slightly bent with respect to the heme (Table 1). For the different subunits, the bending angle varies between 5° and 20°, with an average of 12°. Note that the bending angle depends strongly on the restraints employed. If the bending angle were allowed to vary in an unrestrained fashion, the bending angle would increase to ∼70° (data not shown). The distance from the iron to the nitrogen of NO refined to 1.85 Å, and the distance from the oxygen of NO to the heme pocket water is 2.5 Å. This indicates a strong hydrogen bond (Table 1 and Figure 4C).

Microspectrophotometric Analysis. Figure 5a shows the spectral changes that are observed when a crystal of Cat-5 is exposed to X-rays; Figure 5b shows the same data as difference spectra, and Figure 5c shows how the integrated difference spectra change over time. Over a period of ∼100 s, one sees

Table 1. Data Collection and Refinement Statistics

	CAT-NH_3	CAT-5	CAT-NO
soaking	directly from hanging drop	14 h in NH_3-free buffer	5 min in 100 mM DEANO
a (Å)	83.48	83.22	86.11
b (Å)	140.72	140.92	139.94
c (Å)	229.52	229.37	228.02
$\alpha = \beta = \gamma$ (deg)	90	90	90
space group	$P2_12_12_1$	$P2_12_12_1$	$P2_12_12_1$
volume (Å^3)	2696241.6	2689905.1	2747694.22
resolution (Å)	1.99	1.90	1.88
R_{sym}[a] (last shell)	9.4 (30.3)	8.9 (34.3)	9.1 (32.9)
completeness (last shell) (%)	92.8 (92.8)	97.9 (97.1)	92.2 (89.9)
redundancy (last shell)	5.7 (5.5)	3.6 (3.3)	5.1 (4.3)
I/σ_I (last shell)	5.0 (2.5)	5.1 (2.5)	5.6 (2.1)
R_{crys}/R_{free} without water (%)	23.68/27.05	24.1/26.9	24.05/27.05
no. of water molecules	2126	1277	2013
R_{crys}/R_{free} with water (%)	16.83/20.69	22.16/25.82	18.56/22.05
rmsd for bond lengths[b] (Å)	0.006	0.007	0.006
rmsd for bond angles (deg)	1.3	1.3	1.3

Table 1. Continued

	CAT-NH_3	CAT-5	CAT-NO
no. of Ramachandran outliers	53 (2.9%)	62 (3.3%)	53 (2.9%)
occupancy from electron count (%)			
heme A	70	6.0	51
heme B	71	3.7	40
heme C	82	1.4	35
heme D	95	1.7	74
	80 ± 10	3.2 ± 1.8	50 ± 11
refined occupancy (%)			
heme A	82		55
heme B	100		52
heme C	77		45
heme D	101		61
	90 ± 12.3		53.3 ± 5.8
FE out of plane distance (Å)			
heme A	0.063	0.014	0.016
heme B	−0.054	0.123	−0.035
heme C	−0.044	0.132	−0.020
heme D	−0.052	−0.005	0.019
	−0.02 ± 0.06	0.066 ± 0.07	−0.020 ± 0.027
tilt angle (τ)/bend angle (ϕ)/tilt and bend angle (α) (deg)			
heme A	7.98		9.14/19.6/28.74
heme B	6.01		8.17/5.03/3.13
heme C	0.51		12.28/11.78/24.06
heme D	5.33		8.23/9.72/17.96
	5.0 ± 2.75		9.46 ± 1.68/11.53 ± 5.6/18.47 ± 9.65
rms coordinate error (Å)	0.181	0.262	0.214
iron−nitrogen distance (Å)			
heme A	2.10		1.92
heme B	2.11		1.88
heme C	2.11		1.85
heme D	2.10		1.83
	2.105 ± 0.01		1.87 ± 0.034
nitrogen (NH3)−water oxygen (NO)−water distance (Å)			
heme A	3.05		2.42
heme B	3.05		2.69
heme C	2.96		2.58
heme D	2.76		2.52
	3.0 ± 0.13		2.55 ± 0.11
iron−Tyr distance (Å)			
heme A	2.01	2.00	2.02
heme B	2.00	1.92	1.99
heme C	1.96	1.89	1.96
heme D	2.04	2.01	1.96
	2.0 ± 0.03	2.0 ± 0.06	1.98 ± 0.025
iron−water distance[c] (Å)			
heme A	4.37	4.00	4.27
heme B	4.41		4.20
heme C	4.11		4.25
heme D	4.10	3.98	4.21
	4.25 ± 0.17	3.99 ± 0.01	4.23 ± 0.029

[a] $R_{sym} = \Sigma_i\Sigma_j(I_{i,j} - \langle I\rangle)/(I_{i,j})$. [b] Root-mean-square deviation (rmsd) from ideal geometry. The rmsd values of dihedrals and impropers were 23° and 1°, respectively, for all models. [c] Distance from the heme iron to the closest water molecule near His74.

changes in the visible spectrum characteristic of reduction of heme from the Fe(III) (met) form to the Fe(II) (deoxy) form.[48] Over longer time scales, the area of the integrated difference spectrum decreases, in a process that may indicate crystal

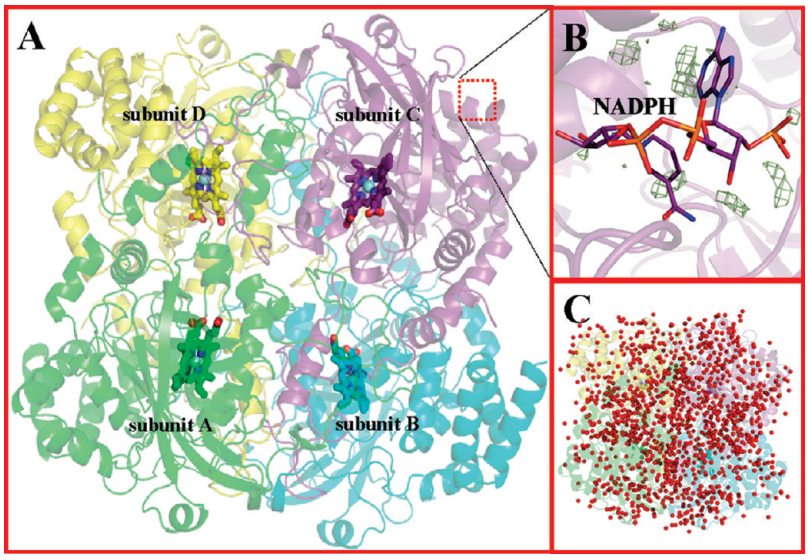

Figure 3. Quaternary structure of beef liver catalase. (A) Cartoon representation, with subunits A−D colored differently; the central heme B is highlighted. The dotted red box highlights the location of an NADPH molecule found in other catalases. (B) Electron density observed in our experiments (green), in the area where other groups have observed NADPH. A putative NADPH molecule is overlaid, showing that the presence of NADPH is not supported. (C) Water structure in the asymmetric unit of CAT-5.

degradation. When the experiment was repeated with other crystals, the rate of the initial increase in the difference spectrum remained fairly invariant, whereas the rate of the subsequent decay varied substantially from one experiment to the next (data not shown).

Panels d−i of Figure 5 are analogous to panels a−c, respectively, except that the observed changes are now for the Cat-NH_3 and Cat-NO crystals, respectively. In the case of Cat-NH_3, the observed spectral changes are somewhat more complicated than those for Cat-5, but they still exhibit features characteristic of heme reduction.[48] The visible spectra of ferrous and ferric heme nitrosyl complexes tend to vary depending on the protein, but a broadening of the signals as seen in Figure 5g is consistent with what is observed when nitrosylated myoglobin[49] or nitrophorin[50] is reduced. Note that the decay in the integrated difference spectrum amplitude that is observed on longer times cales for both the Cat-5 and Cat-NH_3 crystals (Figure 5c,f) is not apparent in the Cat-NO difference spectra (Figure 5i).

The microspectrophotometric data for the three crystal types were obtained over the span of ∼10 min, while 120 min was typically needed to obtain sufficient data for the three crystal structures. Because in each case the spectrophotometric data show that Cat is reduced after 10 min in the X-ray beam, we conclude that in all the crystal structures we obtained the iron centers must be in the +2 oxidation state. However, the cryogenic temperatures that we used would have prevented any major structural changes to the protein in response to the change in metal oxidation state. We are thus confident that the structures reflect the original form of the enzyme, even if the metal was reduced during the experiment.

Kinetic Analysis of Dissociation of NO from Cat-NO. Figure 6a shows the spectral changes observed after a solution initially containing 350 μM BNN, 32 μM MV_{red}, 10 μM Mb, and 15.2 μM Cat had been irradiated with a 308 nm, 10 ns laser pulse. Analysis of the difference spectra by singular-value decomposition (SVD) revealed three spectral components. Subsequent modeling of the spectral changes using the three known extinction coefficient difference spectra, $\Delta\varepsilon_{\text{Cat-NO}}$ ($\varepsilon_{\text{Cat-NO}} - \varepsilon_{\text{Cat}}$), $\Delta\varepsilon_{\text{Mb-NO}}$ ($\varepsilon_{\text{Mb-NO}} - \varepsilon_{\text{Mb}}$), and $\Delta\varepsilon_{\text{MV}}$ ($\varepsilon_{\text{MV}_{\text{red}}} - \varepsilon_{\text{MV}_{\text{ox}}}$),[11,44] allowed us to explain the changes as follows.

The laser pulse produced ∼4.2 μM NO and resulted in an equivalent amount of MV_{red}, as shown in Scheme 2.[a] Within the first few milliseconds of the laser pulse, the free [NO] was reduced to a small, steady-state concentration by reaction with either Cat or Mb. The rate constant for binding of NO to Cat [$k_{on1} = (1.3 \pm 0.1) \times 10^7\ M^{-1}\ s^{-1}$ (Supporting Information)] is comparable to that for binding of NO to Mb ($k_{on2} = 1.7 \times 10^7\ M^{-1}\ s^{-1}$),[49] so comparable amounts of Mb-NO and Cat-NO are generated in this initial phase. From our analysis, we estimate that the initial concentrations of Mb-NO and Cat-NO (the concentrations of each species present when the first spectrum was collected 19 ms after the laser pulse) were 1.9 μM ($[\text{Mb-NO}]_0$) and 2.3 μM ($[\text{Cat-NO}]_0$), respectively.

The binding constant for Mb-NO formation ($K_{\text{Mb-NO}}$) is extremely high (∼10^{11})[49], so binding of NO to Mb can be considered an irreversible process within the time scale of our experiments. Cat also binds NO tightly, but much less so than Mb. Consequently, Cat-NO will release NO within the time scale of our experiments. With these points in mind, the major spectral changes observed in Figure 6a after the first few milliseconds can be attributed to a decrease in [Cat-NO] and a corresponding increase in [Mb-NO], due to the reactions depicted in Scheme 3. These spectral changes were complete within ∼10 s and could be empirically fitted with single exponentials (eq 2 and Figure 6b).

$$\begin{aligned}[\text{Mb-NO}] &= C_{0,1} + A_g(1 - e^{-k_{obs}t}) \\ [\text{Cat-NO}] &= C_{0,2} + A_g e^{-k_{obs}t}\end{aligned} \quad (2)$$

where $C_{0,1}$ and $C_{0,2}$ are constant offsets, A_g is a global amplitude, and k_{obs} is the observed (apparent) rate of the reaction.

Over a longer time scale (60 s), the [Mb-NO] continued to increase at a slow, linear rate, in a process that also consumed MV_{red} (data not shown). We attribute the slower linear process to generation of NO from BNN by the spectrophotometer's

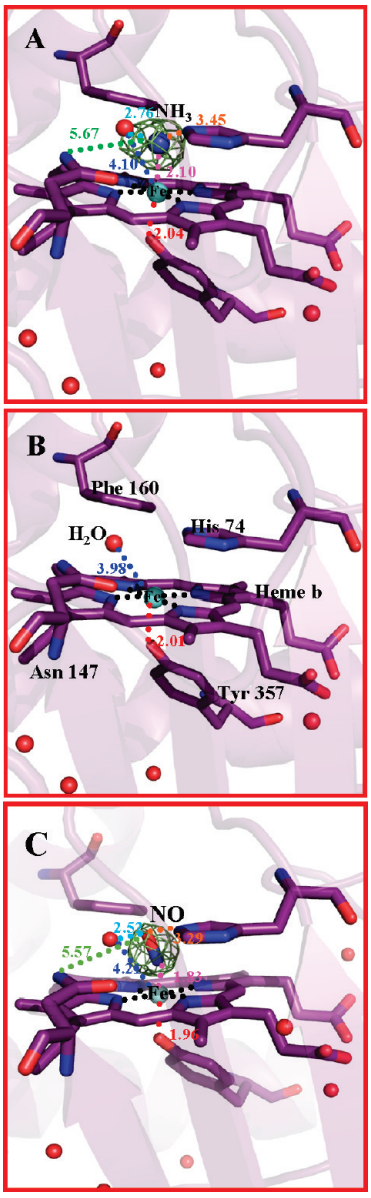

Figure 4. Structure of the heme pocket in the three different Cat forms. Water molecules within 8 Å of the heme iron are shown (red spheres). A sigmaA-weighted $mF_{obs} - DF_{calc}$ simulated annealing difference map is colored green (3.7σ): (A) Cat-NH_3, (B) Cat-5, and (C) Cat-NO. Important heme pocket residues are marked in panel B.

lamp. Note that in Figure 6b the calculated concentration of Cat-NO toward the end of the reaction appears to become negative. We believe this artifact arises mainly because of the uncertainties associated with the extinction coefficient spectra that we used. In particular, we know that there is substantial variation in the published literature values for ε_{Cat}. We generated our ε_{Cat} spectrum from the published value for ε_{Cat} of 1.2×10^5 M^{-1} cm^{-1} at 403 nm (for the monomer), reported by Vlasits et al.[51] However, lower ε_{Cat} values ranging from 1.05×10^5 M^{-1} cm^{-1} [21,34] to 1.07×10^5 M^{-1} cm^{-1} [52] can be found in earlier literature reports. Despite these uncertainties, the increase in [Mb-NO] roughly matches the decrease in [Cat-NO] on the same time scale. Equally importantly, the k_{obs} rate constants obtained by fitting the two concentration versus time traces in Figure 6b agreed within 3% of each other.

Theoretical modeling of the reactions depicted in Scheme 3 shows that the transfer of NO from Cat-NO to Mb-NO is only truly exponential when [Cat] and [Mb] are both much greater than [Cat-NO] and [Mb-NO] (Supporting Information). Nevertheless, the empirical exponential fits of Figure 6b can be used to accurately determine the initial rate for the process ($V_0 = A_g k_{obs}$), which will have the theoretical interpretation shown in eq 3

$$V_0 = \frac{k_{off} k_{on2} [Mb]_0 [Cat\text{-}NO]_0}{k_{on1} [Cat]_0 + k_{on2} [Mb]_0} \quad (3)$$

under all reaction conditions (Supporting Information). k_{on1} and k_{on2} are the on rates of catalase and myoglobin, respecitively, and $[Cat\text{-}NO]_0$ and $[Mb]_0$ are the corresponding concentrations directly after NO is generated (see the Supporting Information). All of the concentrations and parameters in eq 3 except k_{off} are known or were determined experimentally from analysis of the data in Figure 6a. Substituting all the known values into eq 3 and solving for k_{off} yields a value of 1.6 ± 0.3 s^{-1} for the desired parameter.

The experiment depicted in Figure 6 was repeated using a range of Mb and Cat concentrations, and in each case, the value of k_{off} was obtained as described above. As expected, k_{off} exhibited no dependence on the $[Mb]_{tot}/[Cat]_{tot}$ ratio (Figure 7). Averaging all of the k_{off} values shown in Figure 7 gives a best estimate for k_{off} of 1.5 ± 0.1 s^{-1}. From the calculated k_{off} and the value of k_{on1} for binding of NO to Cat (Supporting Information), we estimate the binding constant $K_{Cat\text{-}NO}$ for Cat-NO formation to be $(8.7 \pm 1.2) \times 10^6$. This value is almost 50 times greater than that previously reported by Hoshino et al. (1.8×10^5),[52] but in good agreement with the value of 5.6×10^6 that can be calculated from the reported K_i, for inhibition by NO of catalase's H_2O_2 disproportionation activity.[33] Hoshino et al. obtained their value of $K_{Cat\text{-}NO}$ from NO manometric measurements,[52] which are very difficult to perform at the low pressures required to measure binding constants greater than $\sim 10^5$. We thus feel that our value and that obtained from Brown's K_i value[33] are the more reliable ones. Finally, it should be noted that Hoshino et al. also measured the rate constant k_{on1} for binding of NO to Cat, by photolyzing Cat-NO with a laser pulse and then measuring the rate of NO rebinding in the presence of varying free NO concentrations. Our value for k_{on1} [$(1.3 \pm 0.1) \times 10^7$ M^{-1} s^{-1}] agrees reasonably well with theirs (7.5×10^6 M^{-1} s^{-1} per monomer).[52]

DISCUSSION

Nitric Oxide Binding to Catalase. DEANO is a universal NO generator in powder form (Scheme). It can be easily handled and, because of its high water solubility, can be used to generate large amounts of NO in aqueous solution. With DEANO, the use of the inconvenient, poisonous NO gas tapped from pressurized tanks can be completely avoided, and the amount of NO in solution can be exactly controlled (see also refs 53 and 54). High concentrations of NO dissolved in aqueous solution can be achieved without the vexing pH changes common to gas usage.

In our study of Cat-NO, the use of DEANO and the extremely simple apparatus illustrated in Figure 1 allowed us to expose our crystals to NO concentrations on the order of 100 mM. At 1 bar

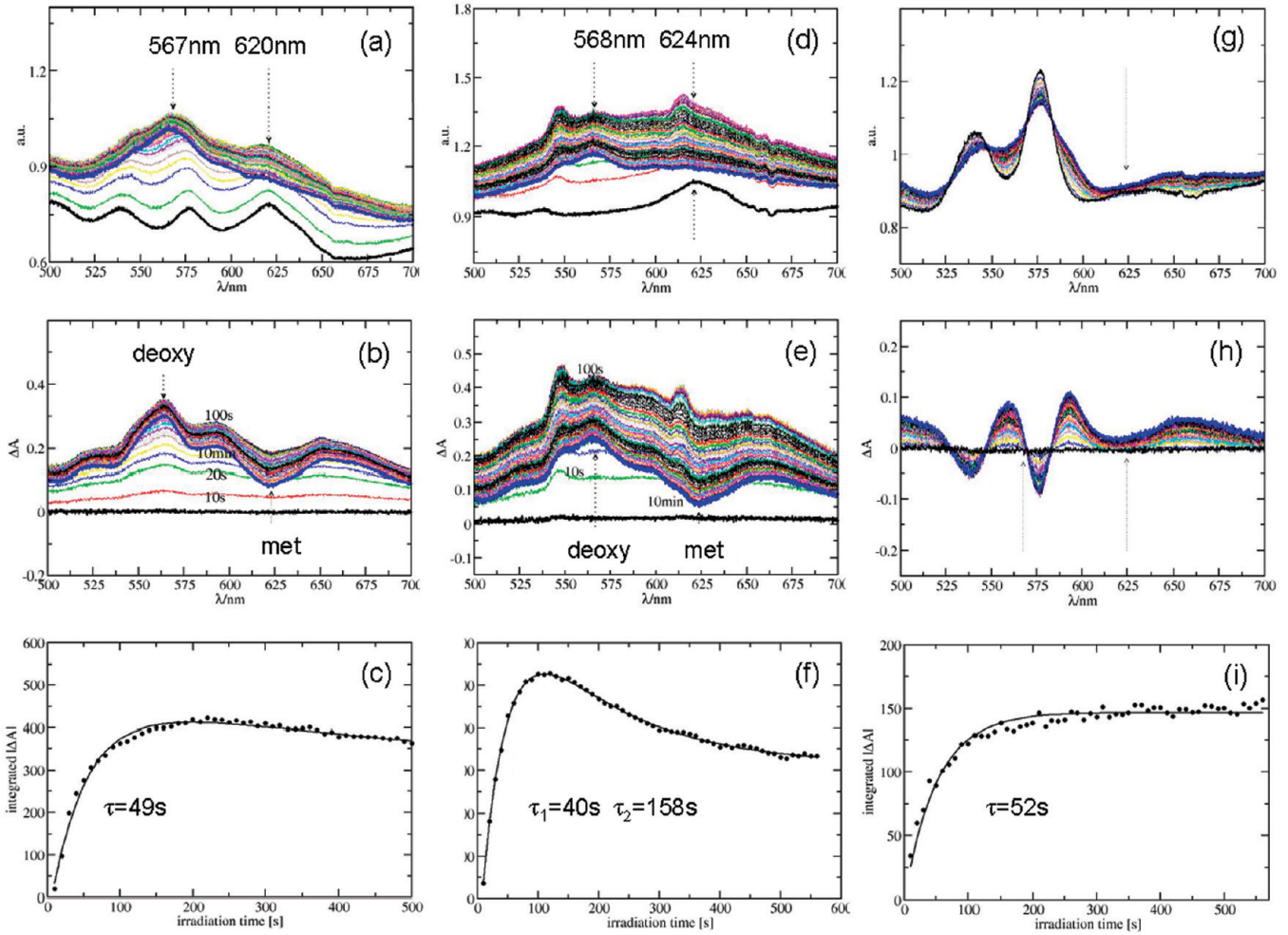

Figure 5. Spectral changes of Cat crystals after X-ray exposure (from 500 to 700 nm). The Soret band region (~410 nm) was excluded, because the high level of absorption of the crystals leads to saturation effects. Panels a, d, and g show spectra for the Cat-5, Cat-NH_3, and Cat-NO crystals, respectively; the thick black lines represent the reference spectra, and the thick blue lines are the spectra after exposure to X-rays for 10 min. Note the disappearance of the met peak around 630 nm and the appearance of deoxy features around 560 nm (dotted arrows) for the Cat-5 and Cat-NH_3 species. Panels b, e, and h show the corresponding difference spectra obtained by subtracting the reference spectra; the thick black lines represent the difference spectra directly after opening the X-ray shutter, and the blue difference spectra were collected after 10 min. The met and deoxy peak positions are again indicated by dotted arrows. Panels c, f, and i show the temporal progression of the changes observed in the integrated difference spectra. Data in panel c were empirically fitted by an exponential and a linear decay. Data in panel f were fitted by two exponentials. Data in panel i were fitted by a single exponential. The characteristic times are indicated.

pressure and 25 °C, the solubility of NO in aqueous solution is 1.93 mM.[55] A 100 mM NO concentration corresponds to a partial pressure of ~50 bar (5 MPa). The NO concentration reached is on the same order of magnitude as the Cat concentration within the crystals. By immersing the catalase crystal in the tightly closed cavity that is completely filled with stabilization buffer, we literally "pressurized" the crystals with NO. It was crucial to start with such high NO concentrations because, though Cat has a relatively large binding constant, it also has a relatively high dissociation rate (k_{off}) of $1.5 \pm 0.1\ s^{-1}$ (Table 2). This means that as soon as the crystals are removed from the NO-containing solution they will quickly begin to lose their bound NO by diffusion. Note that we had to immerse the crystals in NO-free cryobuffer before freezing them in the ice-cold nitrogen gas stream. This procedure took a few seconds, time enough for some NO to diffuse out of the crystal. By initially pressurizing the crystals with NO concentrations much higher than 1 bar, we were still able to detect substantial occupation of NO in the catalase crystals.

Another advantage of our methodology is that with 100 mM DEANO the peak NO concentration reached is ~2 orders of magnitude larger than that of oxygen (O_2 solubility at 25 °C and 1 atm is 1.28 mM).[55] NO normally has to be handled under anaerobic conditions because it reacts very rapidly with O_2. However, in the presence of a large excess of NO, we were able to scrub out the O_2 using only a fraction of the available NO and leaving plenty of NO for the reaction with Cat. Consequently, there was no need to use rigorous anaerobic handling techniques, which greatly complicate crystallographic experiments. Note though that the reaction of O_2 with NO generates acidic products,[56] so even with our methodology the crystals must be buffered with a suitable buffer at a concentration of at least 50 mM to avoid pH changes. The results presented herein will pave the way for easy crystallographic analyses of other proteins that weakly bind NO.

Kinetics of NO Binding. In higher organisms such as mammals, NO is a cell hormone, and its main effect is to increase

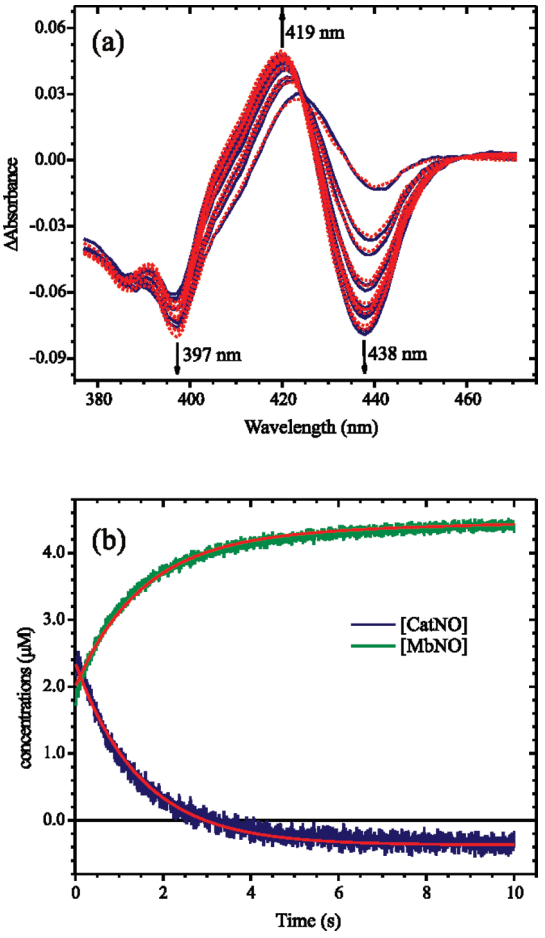

Figure 6. (a) Spectral changes (blue traces) observed after a solution initially containing 350 μM BNN, 32 μM MV_{red}, 10 μM Mb, and 15.2 μM Cat had been irradiated with a 308 nm, 10 ns laser pulse. Calculated difference spectra (red traces) obtained from least-squares fitting of the experimental spectra using the known difference spectra $\Delta\varepsilon_{Mb\text{-}NO}$, $\Delta\varepsilon_{Cat\text{-}NO}$, and $\Delta\varepsilon_{MV}$. (b) Changes in [Cat-NO] and [Mb-NO] as a function of time, calculated from the data fits shown in panel a (green and blue traces, respectively). Least-squares fits (red traces) using exponential functions. The theoretical trace for Mb-NO has a linear component in addition to the exponential one, which becomes noticeable only over longer time scales (data not shown).

Scheme 3

$$\text{CatNO} \underset{k_{on1}}{\overset{k_{off}}{\rightleftharpoons}} \text{Cat} + \text{NO}$$

$$\text{Mb} + \text{NO} \xrightarrow[k_{on2}]{} \text{MbNO}$$

blood flow by vasodilation.[5,8] NO is strongly bound by (ferrous) deoxyhemoglobin (Hb) located in the red blood cells[57] and rapidly oxidized to NO_3^- by oxyhemoglobin (HbO_2),[58,59] processes that normally keep the concentration of NO low in the bloodstream. In tissues, myoglobin takes over the role of hemoglobin in keeping the NO concentration low. Myoglobin, in both its ferric (metMb) and its physiologically more abundant ferrous (Mb) forms, also binds NO.[60,61] The ferrous Mb-NO is remarkably stable with a binding constant $K_{Mb\text{-}NO}$ on the order

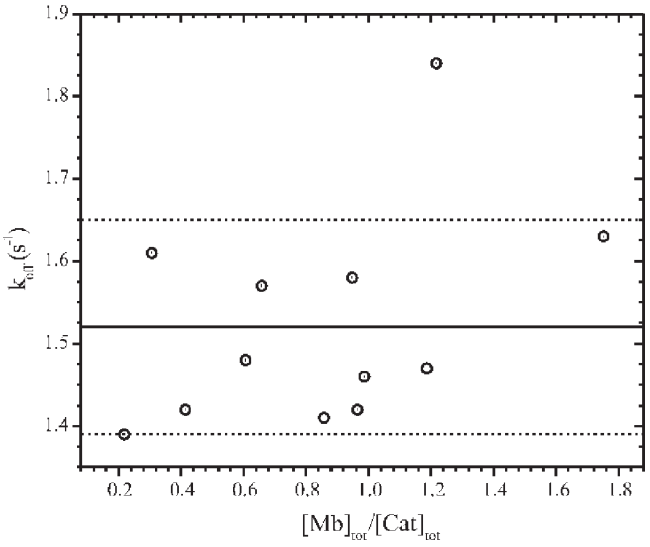

Figure 7. Rate constant values obtained for dissociation of NO from Cat (k_{off}) at different $[Mb]_{tot}/[Cat]_{tot}$ ratios. k_{off} is seen to be independent of $[Mb]_{tot}/[Cat]_{tot}$, which is expected if k_{off} is truly being measured.

Table 2. On and Off Rates and Binding Constants for Several Protein-NO (or CO) Complexes

	k_{on} (M^{-1} s^{-1})	k_{off} (s^{-1})	$K_{Cat\text{-}NO} = k_{on}/k_{off}$ (M^{-1})
$Mb(Fe^{2+})CO$[a]	5.1×10^5	1.9×10^{-2}	2.7×10^7
$Mb(Fe^{2+})NO$[a]	1.7×10^7	1.2×10^{-4}	1.4×10^{11}
$Mb(Fe^{3+})NO$[b]	4.8×10^4	42	1.14×10^3
$Lb(Fe^{2+})NO$[a]	1.2×10^8	2.0×10^{-5}	5.9×10^{12}
$NP1(Fe^{3+})NO$[c]	1.5×10^6 (pH 5)	0.18 (pH 5)	8.3×10^6 (pH 5)
	1.5×10^6 (pH 8)	1.25 (pH 8)	1.2×10^6 (pH 8)
$NP4(Fe^{3+})NO$[c]	2.1×10^6 (pH 5)	0.11 (pH 5)	2.0×10^7 (pH 5)
	2.3×10^6 (pH 8)	1.24 (pH 8)	1.9×10^6 (pH 8)
$Cat(Fe^{3+})NO$[d]	1.3×10^7	1.5	8.7×10^6

[a] From ref 60. Lb is leghemoglobin. [b] From ref 67. [c] From ref 64. The nitrophorins adopt closed and open conformations at pH 5 and 8, respectively. [d] From this work.

of 10^{11} M (Table 2),[49] and like HbO_2, the oxymyoglobin (MbO_2) can oxidize NO to NO_3^-. Thus, Hb and Mb normally keep the NO concentrations in the blood and tissues low, and poisoning of the terminal respiratory cytochrome *c* oxidase with NO is prevented (see ref 62 for the copper B-NO complex of cytochrome *c* oxidase). Uptake of NO through the red blood cells, however, is reportedly[63] slowed by diffusional barriers such as the cell membrane. This can allow transient accumulations of relatively high NO concentrations in the bloodstream, though the impact of such spikes is restricted to a relatively small area. In an example of an event that can transiently increase the NO concentration, blood-sucking insects like the "kissing bug", *Rhodnius prolixus*, inject NO into the host to locally enhance blood flow. To achieve this, the bug uses the heme protein nitrophorin (NP) that contains a ferric central iron to which the NO binds.[64−66] In some nitrophorins, the proximal iron ligand is a cysteine, which may detach from the heme and itself become nitrosylated. This leaves the iron in its ferrous form, which binds NO tightly.[50]

Table 3. Tilt and Bending Angles for NO Found in Different Heme-Iron Proteins with the Iron in Different Oxidation States (NP4, nitrophorin 4)

	tilt and bend angle (deg)		tilt and bend angle (deg)
Mb(Fe^{2+})NO[a]	60	NP4(Fe^{3+})NO[c]	24
Mb(Fe^{3+})NO[a]	33	NP4(Fe^{2+})NO[d]	40
NP4(Fe^{3+})NO[b]	70/3	catalase (Fe^{3+}) (this study)	19

[a] From ref 73. [b] From ref 74. [c] From ref 75. [d] From ref 76.

In general, ferrous iron-containing heme proteins such as Mb and Hb bind NO extremely tightly, with small dissociation rate coefficients [k_{off} (Table 2)]. NO also binds to ferric iron in proteins such as nitrophorin, metMb, and Cat; however, k_{off} values for the ferric compounds are comparably larger, leading to smaller binding constants. In the case of metMb, nitric oxide binds only weakly; the off rate for the ferric form differs from that of the ferrous form by many orders of magnitude.

Like metMb-NO, Cat-NO is comparatively labile; however, $K_{Cat\text{-}NO}$ is substantially higher than $K_{metMb\text{-}NO}$, because of both a higher k_{on} and a lower k_{off} in the case of Cat (Table 2). Our structural investigations reveal potential reasons for these differences. First, metMb has a water molecule bound at the sixth heme coordination site, whereas our data show that Cat-5, the immediate precursor to Cat-NO, has a free sixth position. In metMb nitrosylation, the water molecule must be displaced before NO can enter,[67] which most likely accounts for the higher value of k_{on} for Cat ($1.3 \times 10^7\ M^{-1}\ s^{-1}$) versus that of metMb ($4.8 \times 10^4\ M^{-1}\ s^{-1}$).

Our crystallographic results seem to suggest that the NO in Cat-NO is bent away from the heme normal with angles of ~20° (Table 3). Caution is necessary here, because at the resolution and NO occupancy reached in our experiments the true geometry can be only roughly determined. Nevertheless, slightly bent NO geometries were also found in ferric nitrophorin but not in pure heme-NO adducts where the NO is found to be aligned with the heme normal. In general, ferrous NO complexes tend to have more bent Fe-NO bonds, whereas ferric Fe-NO bonds tend to be more linear.[68] Therefore, our crystallographic data seem to be consistent with the heme having somewhat reduced character. This in turn is consistent with our microspectrophotometric data, which show that Cat is photoreduced in the X-ray beam; however, at the low temperature at which the data were collected (100 K), very little atomic rearrangement can occur within a molecule, so we suspect that the Cat-NO structure represents a metastable ferrous form in which the Fe-NO bond is "frozen in the ferric" arrangement. If so, then, in a catalase that has never been exposed to any X-rays, the Fe-NO bending angle would suggest that the heme iron in Cat has some ferrous character, despite being formally Fe(III). Such behavior has been observed in model systems.[68] Depending on the amount of extra density supplied, the iron gains Fe(II) character. The bend increases the degree of orbital overlap of NO with the molecular orbitals of the iron/protoporphyrin system,[68] which in turn decreases the dissociation rate relative to that of metMb. A final factor that could stabilize the NO in Cat relative to metMb-NO is the water molecule that sits nearby and may form a hydrogen bond to the oxygen of NO, bending and stabilizing it further (Figure 4C).

Possible Implications for Catalysis of H_2O_2 Disproportionation. H_2O_2 is both an oxidizing and a reducing agent. Catalase

Table 4. Structural Differences in Angstroms Relative to CAT-5 (no sixth iron ligand) Averaged over All Four Subunits

	CAT-NH_3	CAT-NO
heme Fe and N atoms	0.1 ± 0.01	0.1 ± 0.01
proximal side of the heme		
Tyr357 O_η	0.11 ± 0.02	0.14 ± 0.04
distal side of the heme		
His74 $N_{\delta1}/N_{\varepsilon2}$	0.12 ± 0.06	0.14 ± 0.06
Asn147 $O_{\delta1}/N_{\delta2}$	0.12 ± 0.07	0.16 ± 0.08
Phe160 C_ζ	0.15 ± 0.03	0.13 ± 0.07
total rms difference[a]	0.34 ± 0.04	0.37 ± 0.05

[a] The structures were superimposed by a least-squares fit (Xfit[41]).

works by transferring a total of four electrons, in two different steps, at a rate of two electrons per step. First, two electrons are transferred to one molecule of H_2O_2, and then two electrons are accepted from a second H_2O_2 according to

$$\text{porphyrin-Fe(III)} + H_2O_2 \rightarrow \text{porphyrin}^{+\bullet}\text{-Fe(IV)} = O + H_2O \quad (4)$$

$$\text{porphyrin}^{+\bullet}\text{-Fe(IV)} = O + H_2O_2 \rightarrow \text{porphyrin-Fe(III)} + H_2O + O_2 \quad (5)$$

The oxyferryl-porphyrin complex generated by eq 4 is called compound I. In the Fita−Rossman model,[34] the oxoferryl attacks another H_2O_2 molecule abstracting a hydride ion. We are left with an OH^- at the iron. The iron itself again becomes Fe(III), and one electron is transferred back to the porphyrin. Another proton is temporarily stored at the N_ε atom of the distal heme pocket His74 and finally transferred to the OH^- at the iron to form water. This water binds only weakly to the catalase iron and is quickly released. Other mechanisms without the involvement of His74 have also been proposed.[69] Reaction 4 requires that the porphyrin-Fe(III) complex easily donate electrons; hence, it acts as a reducing agent. This is not conceivable unless there is evidence that this complex has an excess of electron density. Our putatively bent NO suggests that the iron has iron(II) character, which is obtained from binding the negatively charged hydroxyl oxygen of the proximal ligand tyrosine (see the discussion above). This largely will facilitate the formation of compound I and contributes to the speed of the catalase.

Our NO catalase seems to be good model for mimicking the Fe(H_2O_2) adduct, with NO taking the place of H_2O_2. The water molecule that appears ~4 Å from the Fe in all three structures, and is strongly H-bonded to the NO, could facilitate oxoferryl production in the H_2O_2 adduct by donating a proton to the incipient water being formed in reaction 4. The nearby water could also mark the spot where the second H_2O_2 sits to interact with both the distal His74 and the oxoferryl in reaction 5.

Note that the structural changes in catalase that accompany changes in coordination at the Fe distal site are minute. The iron out of plane distance is almost zero regardless of whether there is a distal ligand such as NO or NH_3 (Table 4). The positions of all distal and proximal residues remain essentially unchanged within the coordinate error of our structure analysis [~0.18 Å (Table 1)]. Similar results are also observed upon ligand binding in a bacterial catalase.[30] Catalase's rigidity through the catalytic

Table 5. Cavities in Selected Proteins[a]

	no. of cavities	H_2O in cavity/ total H_2O	%	PDB entry
catalase[b]	140	100/1277	8	this work
catalase (human, 1.5 Å)[c]	108	197/2298	9	1DGF
cytochrome *c* oxidase[d]	95	85/1579	5	3ABK
L29W deoxyMb[e]	2	1/100	1	2BLI
deoxyMb (to 1.15 Å)[f]	2	0	0	1A6N

[a] Calculations were conducted using "voidoo"[77] using a probe with a radius of 1.4 Å on a 0.5 Å grid. [b] Cat-5, from this study. [c] From ref 32. [d] From ref 62. [e] From ref 43. [f] From ref 72.

cycle seems to be designed to make it an effective electron transfer protein where structural changes remain as small as possible, optimized for speed. In contrast, in myoglobin, the iron moves out the heme plane by ~0.3 Å and the heme itself domes once the distal ligand is removed.[42,43] Large structural changes are triggered by this relaxation. Another possibly important feature of catalase is that it is internally wet. We identified ~1280 water molecules; ~100 (8%) are located in 140 cavities within the protein matrix (Table 5 and Figure 3C). In a protein similar in size, cytochrome *c* oxidase, whose structure has been determined to similar resolution,[62] 5% of the water can be found in 108 cavities. In terms of electron transfer and substrate diffusion, the terminal oxidase and catalase have similar functions. This seems to be reflected in the vast number of cavities. The importance of cavities for substrate diffusion and storage was outlined extensively for myoglobin.[43,70,71] Myoglobin, however, has only a few cavities in which <1% of the water can be found, even at atomic resolution.[72] Catalase can effectively guide the substrate through the network of cavities to its active center to cope with the high turnover rates.

■ ASSOCIATED CONTENT

Supporting Information. Determination of k_{on1} for the binding of NO to Cat and theoretical analysis of the experiments in which NO was photogenerated in the presence of both Cat and Mb. This material is available free of charge via the Internet at http://pubs.acs.org.

Accession Codes

The coordinates and structure factor amplitudes for Cat-NH_3, Cat-5, and Cat-NO complexes were deposited in the Protein Data Bank as entries 3RGS, 3RE8, and 3RGP, respectively.

■ AUTHOR INFORMATION

Corresponding Author

*M.S.: Department of Physics, University of Wisconsin—Milwaukee, 1900 E. Kenwood Blvd., Milwaukee, WI 53211; phone, (414) 229-4338; fax, (414) 229-5589; e-mail, m-schmidt@uwm.edu. A.A.P.: Department of Chemistry and Biochemistry, University of Wisconsin—Milwaukee, 3210 N. Cramer St., Milwaukee, WI 53211; phone, (414) 229-4413; fax, (414) 229-5530; e-mail, apacheco@uwm.edu.

Notes

[a]Actually, as explained in ref 11, the amount of MV_{red} oxidized is slightly smaller than the amount of NO generated. The $[MV_{ox}]/[NO]$ ratio is known and can be used to independently estimate the amount of NO generated by the laser pulse.

Funding Sources

A.A.P. and M.S. are supported by National Science Foundation (NSF) Grant 0843459 and the University of Wisconsin—Milwaukee's Research Growth Initiative (Grant 101X157). M.S. is also supported by NSF CAREER Grant 0952643.

■ ACKNOWLEDGMENT

We thank Vukica Srajer and Yu-Sheng Chen at BioCARS for constant support during all phases of data collection. Use of BioCARS Sector 14 was supported by the National Institutes of Health, National Center for Research Resources, via Grant RR007707.

■ ABBREVIATIONS

BNN, *N*,*N*′-bis(carboxymethyl)-*N*,*N*′-dinitroso-*p*-phenylenediamine; Cat, catalase; DEANO, 1-(*N*,*N*-diethylamino)diazen-1-ium-1,2-diolate; Mb, myoglobin; MV (MV_{ox}), methyl viologen; MV_{red}, methyl viologen monocation radical; NADPH, nicotinamide adenine dinucleotide phosphate (reduced); NO, nitric oxide.

■ REFERENCES

(1) Hibbs, J. B., Vavrin, Z., and Taintor, R. R. (1987) L-Arginine Is Required for Expression of the Activated Macrophage Effector Mechanism Causing Selective Metabolic Inhibition in Target Cells. *J. Immunol. 138*, 550–565.

(2) Moncada, S., Palmer, R. M. J., and Higgs, E. A. (1989) Biosynthesis of Nitric oxide from L-Arginine. *Biochem. Pharmacol. 38*, 1709–1715.

(3) Bult, H., Boeckxstaens, G. E., Pelckmans, P. A., Jordaens, F. H., Van Maercke, Y. M., and Herman, A. G. (1990) Nitric Oxide as an Inhibitory Non-Adrenergic Non-Cholinergic Neurotransmitter. *Nature 345*, 346–347.

(4) Shibuki, K., and Okada, D. (1991) Endogenous nitric oxide release required for long-term synaptic depression in the cerebellum. *Nature 349*, 326–328.

(5) Bredt, D. S., Hwang, P. M., Glatt, C. E., Lowenstein, C., Reed, R. R., and Snyder, S. H. (1991) Cloned and expressed nitric oxide synthase structurally resembles cytochrome P-450 reductase. *Nature 351*, 714–718.

(6) Heck, D. E., Laskin, D. L., Gardner, C. R., and Laskin, J. D. (1992) Epidermal Growth Factor Suppresses Nitric Oxide and Hydrogen Peroxide production by Keratinocytes (Potential Role for Nitric Oxide in the Regulation of Wound healing). *J. Biol. Chem. 267*, 21277–21280.

(7) Ford, P. C., and Lorkovic, I. M. (2002) Mechanistic aspects of the reactions of nitric oxide with transition-metal complexes. *Chem. Rev. 102*, 993–1017.

(8) Stamler, J. S., Lamas, S., and Fang, F. C. (2001) Nitrosylation: The protoypic redox-base signaling mechanism. *Cell 106*, 675–683.

(9) Matsumoto, A., Comatas, K. E., Liu, L., and Stamler, J. S. (2003) Screening for Nitric Oxide-dependent protein-protein interactions. *Science 301*, 657–661.

(10) Richter-Addo, G. B., Legzdins, P., and Burstyn, J. (2002) Introduction: Nitric oxide chemistry. *Chem. Rev. 102*, 857–860.

(11) Cabail, M. Z., Moua, V., Bae, E., Meyer, A., and Pacheco, A. A. (2007) Quantifying the photoinduced release of nitric oxide from N,N'-bis(carboxymethyl)-N,N′-dinitroso-1,4-phenylenediamine. Effect of reducing agents on the mechanism of the photoinduced reactions. *J. Phys. Chem. A 111*, 1207–1213.

(12) Bodemer, G., Ellis, L. M., Lace, P. J., Mooren, P. E., Patel, N. K., Ver Haag, M., and Pacheco, A. A. (2004) Photochemically-induced

reduction and rearrangements of N,N′-bis-(carboxymethyl)-N,N′-dinitroso-1,4-phenylenediamine. *J. Photochem. Photobiol., A 163*, 53–60.

(13) Cabail, M. Z., Lace, P. J., Uselding, J., and Pacheco, A. A. (2002) Kinetic studies of the photoinitiated NO-releasing reactions of N,N′-bis-(carboxymethyl)-N,N′-dinitroso-1,4-phenylenediamine. *J. Photochem. Photobiol., A 152*, 109–121.

(14) Murthy, M. R. N., Reid, T. J., Sicignano, A., Tanaka, N., and Rossmann, M. G. (1981) Structure of beef liver catalase. *J. Mol. Biol. 152*, 465–499.

(15) Aebi, H. (1984) Catalase in vitro. *Methods Enzymol. 105*, 121–127.

(16) Halliwell, B., and Gutteridge, J. M. C. (1990) Role of free radicals and catalytic metal ions in human disease: An overview. *Methods Enzymol. 186*, 1–85.

(17) Michiels, C., Raes, M., Toussaint, O., and Remacle, J. (1994) Importance of Se-glutathione peroxidase, catalase, and Cu/Zn-SOD for cell survival against oxidative stress. *Free Radical Biol. Med. 17*, 235–248.

(18) Ko, T. P., Safo, M. K., Musayev, F. N., Di Salvo, M. L., Wang, C. Q., Wu, S. H., and Abraham, D. J. (2000) Structure of human erythrocyte catalase. *Acta Crystallogr. D56*, 241–245.

(19) Sumner, J. B., and Dounce, A. L. (1937) Crystalline catalase. *J. Biol. Chem. 121*, 417–424.

(20) Deisseroth, A., and Dounce, A. L. (1969) The purification and crystallization of beef liver erythrocyte catalase. *Arch. Biochem. Biophys. 131*, 18–29.

(21) Reid, T. J., Murthy, M. R. N., Sicignano, A., Tanaka, N., Musick, W. D. L., and Rossmann, M. G. (1981) Structure and heme environment of beef liver catalase at 2.5 Å resolution. *Proc. Natl. Acad. Sci. U.S.A. 78*, 4767–4771.

(22) Ko, T. P., Day, J., Malkin, A. J., and McPherson, A. (1999) Structure of orthorhombic crystals of beef liver catalase. *Acta Crystallogr. D55*, 1383–1394.

(23) Tanford, C., and Lovrien, R. (1962) Dissocation of catalase into subunits. *J. Am. Chem. Soc. 84*, 1892–1896.

(24) Sund, H., Weber, K., and Molbert, E. (1967) Dissocation of beef liver catalase in its subunits. *Eur. J. Biochem. 1*, 400–410.

(25) Torii, K., Iizuka, T., and Ogura, Y. (1970) Magnetic susceptibility and EPR measurements of catalase and its derivatives. A thermal equilibrium between the high- and low-spin states in the catalase-azide compound. *J. Biochem. 68*, 837–841.

(26) Stern, K. G. (1936) The constitution of the prosthetic group of catalase. *J. Biol. Chem. 112*, 661–669.

(27) Schroeder, W. A., Shelton, J. R., Shelton, J. B., Robberson, B., Apell, G., Fang, R. S., and Bonaventura, J. (1982) The complete amino acid sequence of bovine liver catalase and the partial sequence of bovine erythrocyte catalase. *Arch. Biochem. Biophys. 214*, 397–421.

(28) Murshudov, G. N., Grebenko, A. I., Brannigan, J. A., Antson, A. A., Barynin, V., Dodson, G. G., Dauter, Z., Wilson, K. S., and Melik-Adamyan, W. R. (2002) The structures of *Micrococcus lysodeikticus* catalase, its ferryl intermediate (compound II) and NADPH complex. *Acta Crystallogr. D58*, 1972–1982.

(29) Andreoletti, P., Sainz, G., Jaquinod, M., Gagnon, J., and Jouve, H. M. (2003) High-resolution structure and biochemical properties of a recombinant *Proteus mirabilas* catalase depleted in iron. *Proteins: Struct., Funct., Genet. 50*, 261–271.

(30) Gouet, P., Jouve, H.-M., Williams, P. A., Andersson, I., Andreoletti, P., Nussaume, L., and Hajdu, J. (1996) Ferryl intermediates of catalase captured by time-resolved Weissenberg crystallography and UV/Vis spectroscopy. *Nat. Struct. Biol. 3*, 951–956.

(31) Alfonso-Prieto, M., Borovik, A., Carpena, X., Murshudov, G., Melik-Adamyan, W., Fita, I., Rovira, C., and Loewen, P. C. (2007) The structures and electronic configuration of compound I intermediates of *Helicobacter pylori* and *Penicillium vitale* catalases determined by X-ray crystallography and QM/MM density functional theory calculations. *J. Am. Chem. Soc. 129*, 4193–4205.

(32) Putnam, C. D., Arvai, A. S., Bourne, Y., and Tainer, J. A. (2000) Active and inhibited human catalase structures: Ligand and NADPH binding and catalytic mechanism. *J. Mol. Biol. 296*, 295–309.

(33) Brown, G. C. (1995) Reversible Binding and Inhibition of Catalase by Nitric-Oxide. *Eur. J. Biochem. 232*, 188–191.

(34) Fita, I., and Rossmann, M. G. (1985) The NADPH binding site of beef liver catalase. *Proc. Natl. Acad. Sci. U.S.A. 82*, 1604–1608.

(35) Drago, R. S., and Paulik, F. E. (1960) The Reaction of Nitrogen(II) Oxide with Diethylamine. *J. Am. Chem. Soc. 82*, 96–98.

(36) Leslie, A. G. (2006) The integration of macromolecular diffraction data. *Acta Crystallogr. D62*, 48–57.

(37) Evans, P. (2006) Scaling and assessment of data quality. *Acta Crystallogr. D62*, 72–82.

(38) Kabsch, W. (1988) Evaluation of single-crystal X-ray diffraction data from a position-sensitive detector. *J. Appl. Crystallogr. 21*, 916–924.

(39) Berman, H. M., Westbrook, J., Feng, Z., Gilliland, G., Bhat, T. N., Weissig, H., Shindyalov, I. N., and Bourne, P. E. (2000) The protein data bank. *Nucleic Acids Res. 28*, 235–242.

(40) Bruenger, A. T., Adams, P. D., Clore, G. M., Delano, W. L., Gros, P., Gross-Kunstleve, R. W., Jiang, J. S., Kuszewski, J., Nilges, M., Pannu, N. S., Read, R. J., Rice, L. M., Simonoson, T., and Warren, G. L. (1988) Crystallography and NMR system: A new software suite for macromolecular structure determination. *Acta Crystallogr. D54*, 905–921.

(41) McRee, D. E. (1999) XtalView Xfit: A versatile program for manipulating atomic coordinates and electron density. *J. Struct. Biol. 125*, 156–165.

(42) Srajer, V., Ren, Z., Teng, T., Schmidt, M., Ursby, T., Bourgeosis, D., Pradervand, C., Schildkamp, W., Wulff, M., and Moffat, K. (2001) Protein conformational relaxation and ligand migration in myoglobin: A nanosecond to millisecond molecular movie from time-resolved Laue X-ray diffraction. *Biochemistry 40*, 13802–13815.

(43) Nienhaus, K., Ostermann, A., Nienhaus, G. U., Paraka, F. G., and Schmidt, M. (2005) Ligand migration and protein fluctuations in myoglobin mutant L29W. *Biochemistry 44*, 5095–5105.

(44) Kostera, J., Youngblut, M. D., Slosarczyk, J. M., and Pacheco, A. A. (2008) Kinetic and product distribution analysis of NO reductase activity in *Nitrosomonas europaea* hydroxylamine oxidoreductase. *J. Biol. Inorg. Chem. 13*, 1073–1083.

(45) Namiki, S., Arai, T., and Fujimori, K. (1997) High-performance caged nitric oxide: A new molecular design, synthesis, and photochemical reaction. *J. Am. Chem. Soc. 119*, 3840–3841.

(46) Kirkman, H. N., and Gaetani, G. F. (1984) Catalase: A tetrameric enzyme with four tightly bound molecules of NADPH. *Proc. Natl. Acad. Sci. U.S.A. 81*, 4343–4347.

(47) Drenth, J. (1994) *Principles of Protein X-ray Crystallography*, Springer, New York.

(48) Shimizu, N., Kobayashi, K., and Hayashi, K. (1988) Studies on the Equilibria and Kinetics of the Reactions of Ferrous Catalase with Ligands. *J. Biochem. 104*, 136–140.

(49) Hoshino, M., Maeda, M., Konishi, R., Seki, H., and Ford, P. C. (1996) Studies on the reaction mechanism for reductive nitrosylation of ferrihemoproteins in buffer solutions. *J. Am. Chem. Soc. 118*, 5702–5707.

(50) Weichsel, A., Maes, E. M., Andersen, J. F., Valenzuela, J. G., Shokhireva, T., Walker, F. A., and Montfort, W. R. (2005) Heme-assisted S-nitrosation of a proximal thiolate in a nitric oxide transport protein. *Proc. Natl. Acad. Sci. U.S.A. 102*, 594–599.

(51) Vlasits, J., Jakopitsch, C., Schwanninger, M., Holubar, P., and Obinger, C. (2007) Hydrogen peroxide oxidation by catalase-peroxidase follows a non-scrambling mechanism. *FEBS Lett. 581*, 320–324.

(52) Hoshino, M., Ozawa, K., Seki, H., and Ford, P. C. (1993) Photochemistry of Nitric-Oxide Adducts of Water-Soluble Iron(III) Porphyrin and Ferrihemoproteins Studied by Nanosecond Laser Photolysis. *J. Am. Chem. Soc. 115*, 9568–9575.

(53) Schreiter, E. R., Rodriguez, M. M., Weichsel, A., Montfort, W. R., and Bonaventura, J. (2007) S-Nytrosylation-induced Conformational Change in Blackfin Tuna Myoglobin. *J. Biol. Chem. 282*, 19773–19780.

(54) Ma, X., Sayed, N., Beuve, A., and van den Akker, F. (2007) NO and CO differentially activate soluble guanylyl cyclase via a heme pivot-bend mechanism. *EMBO J. 26*, 578–588.

(55) Wilhelm, E., Battino, R., and Wilcock, R. J. (1977) Low-pressure solubility of gases in liquid water. *Chem. Rev. 77*, 219–262.
(56) Cotton, F. A., Wilkinson, G., Murillo, C. A., and Bochmann, M. (1999) *Advanced Inorganic Chemistry*, 6th ed., pp 309−379, John Wiley and Sons, Inc., New York.
(57) Kim-Shapiro, D. B., Schechter, A. N., and Gladwin, M. T. (2006) Unraveling the reactions of nitric oxide, nitrite, and hemoglobin in physiology and therapeutics. *Arterioscler. Thromb. Vasc. Biol. 26*, 697–705.
(58) Herold, S., Exner, M., and Nauser, T. (2001) Kinetic and Mechanistic Studies of the NO-Mediated Oxidation of Oxymyoglobin and Oxyhemoglobin. *Biochemistry 40*, 3385–3395.
(59) Eich, R. F., Li, T., Lemon, D. D., Doherty, D. H., Curry, S. R., Aitken, J. F., Mathews, A. J., Johnson, K. A., Smith, R. D., Phillips, G. N., and Olson, J. S. (1996) Mechanism of NO-induced oxidation of myoglobin and hemoglobin. *Biochemistry 35*, 6976–6983.
(60) Rohlfs, R. J., Gibson, J. S., and Gibson, O. H. (1988) A comparison of the geminate recombination kinetics of several monomeric heme proteins. *J. Biol. Chem. 263*, 1803–1813.
(61) Miller, L. M., Pedraza, A. J., and Chance, M. R. (1997) Identification of Conformational Substates Involved in Nitric Oxide Binding to Ferric and Ferrous Myoglobin through Difference Fourier Transform Infrared Spectroscopy (FTIR). *Biochemistry 36*, 12199–12207.
(62) Ohta, K., Muramoto, K., Shinzawa-Itoh, K., Yamashita, E., Yoshikawa, S., and Tsukihara, T. (2010) X-ray structure of the NO-bound copper B in the bovine cytochrome-c oxidase. *Acta Crystallogr. F66*, 251.
(63) Gladwin, M. T., and Patel, R. P. (2008) The Role of Red Blood Cells and Hemoglobin−Nitric Oxide Interactions on Blood Flow. *Am. J. Respir. Cell Mol. Biol. 38*, 125–126.
(64) Andersen, J. F., Ding, X. D., Balfour, C., Shokhireva, T. K., Champagne, D. E., Walker, F. A., and Montfort, W. R. (2000) Kinetics and equilibria in ligand binding by nitrophorins 1−4: Evidence for stabilization of a nitric oxide-ferriheme complex through a ligand-induced conformational trap. *Biochemistry 39*, 10118–10131.
(65) Nienhaus, K., Maes, E. M., Weichsel, A., Montfort, W. R., and Nienhaus, G. U. (2004) Structural dynamics controls nitric oxide affinity in nitrophorin 4. *J. Biol. Chem. 279*, 39401–39407.
(66) Kondrashov, D. A., Roberts, S. A., Weichsel, A., and Montfort, W. R. (2004) Protein functional cycle viewed at atomic resolution: Conformational change and mobility in nitrophorin 4 as a function of pH and NO binding. *Biochemistry 43*, 13637–13647.
(67) Laverman, L. E., Wanat, A., Oszajca, J., Stochel, G., Ford, P. C., and van Eldik, R. (2001) Mechanistic studies on the reversible binding of nitric oxide to metmyoglobin. *J. Am. Chem. Soc. 123*, 285–293.
(68) Richter-Addo, G. B., Wheeler, R. A., Hixson, C. A., Chen, L., Khan, M. A., Ellison, M. K., Schulz, C. E., and Scheidt, W. R. (2001) Unexpected Nitrosyl-Group Bending in Six-Coordinate $\{M(NO)\}^6$ σ-Bonded Aryl(iron) and -(ruthenium) Porphyrins. *J. Am. Chem. Soc. 123*, 6314–6326.
(69) Alfonso-Prieto, M., Biarnes, X., Vidossich, P., and Rovira, C. (2009) The molecular mechanism of the catalase reaction. *J. Am. Chem. Soc. 131*, 11751–11761.
(70) Tilton, R. F., Kuntz, I. D., and Petsko, G. A. (1984) Cavities in proteins: Structure of a metmyoglobin-xenon complex solved to 1.9 Å. *Biochemistry 23*, 2849–2857.
(71) Ostermann, A., Waschipky, R., Parak, F. G., and Nienhaus, G. U. (2000) Ligand binding and conformational motions in myoglobin. *Nature 404*, 205–208.
(72) Vojtechovský, J., Chu, K., Berendzen, J., Sweet, R. M., and Schlichting, I. (1999) Crystal structures of myoglobin-ligand complexes at near-atomic resolution. *Biophys. J. 77*, 2153–2174.
(73) Copeland, D. M., West, A. H., and Richter-Addo, G. B. (2003) Crystal Structures of Ferrous Horse Heart Myoglobin Complexed with Nitric Oxide and Nitrosoethane. *Proteins: Struct., Funct., Genet. 53*, 182–192.
(74) Weichsel, A., Andersen, J. F., Roberts, S. A., and Montfort, W. R. (2000) Nitric oxide binding to nitrophorin 4 induces complete distal pocket burial. *Nat. Struct. Biol. 7*, 551–554.
(75) Roberts, S. A., Weichsel, A., Qiu, Y., Shelnutt, J. A., Walker, F. A., and Montfort, W. R. (2001) Ligand-induced heme ruffling and bent NO geometry in ultra-high-resolution structures of nitrophorin 4. *Biochemistry 40*, 11327–11337.
(76) Maes, E. M., Roberts, S. A., Weichsel, A., and Montfort, W. R. (2005) Ultrahigh resolution structures of nitrophorin 4: Heme distortion in ferrous CO and NO complexes. *Biochemistry 44*, 12690–12699.
(77) Kleywegt, G. J., and Jones, T. A. (1994) Detection, delineation, measurement and display of cavities in macromolecular structures. *Acta Crystallogr. D50*, 178–185.